

Ferrocene-functionalized covalent organic framework exceeding the ultimate hydrogen storage targets: a first-principles multiscale computational study

Marcus Djokic¹ and Jose L. Mendoza-Cortes^{1, 2, *}

¹*Department of Chemical Engineering and Material Science,
Michigan State University, East Lansing, MI 48824, USA*

²*Department of Physics and Astronomy, Michigan State University, East Lansing, MI 48824, USA*

The development of efficient hydrogen storage materials is crucial for advancing the hydrogen economy and meeting the U.S. Department of Energy's targets of 6.5 wt% and 50 g H₂ L⁻¹ for automotive applications. We present a computational study of ferrocene-functionalized covalent organic frameworks (COFs) for hydrogen storage. Following the **Multi-binding Sites United in Covalent-Organic Framework (MSUCOF)** approach, we introduce MSUCOF-4-FeCp, designed by incorporating ferrocene (FeCp₂) moieties into IRCOF-102. Notably, it achieves exceptional performance with gravimetric and volumetric uptakes of 18.0 wt% and 72.6 g H₂ L⁻¹ at 298 K and 700 bar. The material exhibits optimal binding energies (15–20 kJ·mol⁻¹) ensuring both high storage capacity and deliverable hydrogen under practical conditions. This work establishes ferrocene functionalization as a cost-effective alternative to precious metal incorporation in COFs.

I. INTRODUCTION

The urgent need for sustainable energy solutions positions hydrogen as a promising clean energy carrier, capable of addressing both energy security and environmental concerns associated with the dependence on fossil fuels. However, the widespread adoption of hydrogen as a transportation fuel faces significant challenges, particularly in developing safe, efficient, and cost-effective storage systems. The U.S. Department of Energy (DOE) has established ambitious targets for hydrogen storage in light-duty vehicles: 6.5 wt% gravimetric capacity and 50 g H₂ L⁻¹ volumetric capacity, with the overarching goal of reducing clean hydrogen costs to \$1 per kilogram by 2031.[1, 2]

A. Covalent organic frameworks for hydrogen storage

Covalent organic frameworks (COFs) have emerged as particularly promising candidates for hydrogen storage applications due to their high surface areas, tunable pore structures, and composition primarily of light elements.[3] Unlike their metal-organic framework (MOF) counterparts, COFs offer the advantage of lower framework density while maintaining structural integrity and thermal stability. The crystalline nature of COFs allows for precise control over the size and functionality of pores, allowing rational design approaches to optimize their hydrogen uptake properties.[4, 5]

Recent advances in COF chemistry have demonstrated that hydrogen storage performance can be significantly enhanced through strategic incorporation of functional groups and heteroatoms.[6, 7] The introduction of open metal sites and polarizing groups has been shown to

strengthen van der Waals interactions with hydrogen molecules, thus improving binding enthalpies and storage capacities.[8, 9] However, achieving the optimal balance between gravimetric and volumetric performance remains a central challenge, as strategies to increase volumetric uptake often lead to increased framework density and reduced gravimetric capacity.[10]

B. Metallocene chemistry and hydrogen binding

Metallocenes represent a unique class of organometallic compounds characterized by their distinctive "sandwich" structure, where a central metal atom is coordinated to two cyclic organic ligands. The discovery of ferrocene in 1951 by Kealy and Pauson[19] revolutionized organometallic chemistry and earned its structural elucidators, Geoffrey Wilkinson[20] and Ernst Otto Fischer[21], the 1973 Nobel Prize in Chemistry.[22] Ferrocene (Fe(*n*⁵-C₅H₅)₂) exhibits remarkable thermal stability (stable to 400°C), chemical inertness, and well-defined electrochemical properties with a reversible Fe²⁺/Fe³⁺ redox couple at +0.4 V *vs.* SCE.[23]

The electronic structure of ferrocene, governed by the 18-electron rule, provides multiple potential binding sites for small molecules; these binding sites have been exploited across various porous materials. Ferrocene-functionalized MOFs have already been synthesized, utilizing the redox-active iron center to enable photocatalytic reduction of CO₂ with enhanced electron transfer capabilities.[24] Similarly, microporous polymers containing ferrocene demonstrate improved storage of CO₂ through the synergistic effects of microporosity and metal-ligand interactions.[25] Analogously, superior hydrogen storage performance has also been reported for carbon foams loaded with ferrocene.[26]

The versatility of ferrocene extends beyond simple gas adsorption: it fundamentally alters electronic density distributions, spatial arrangements, and coordination en-

* jmendoza@msu.edu

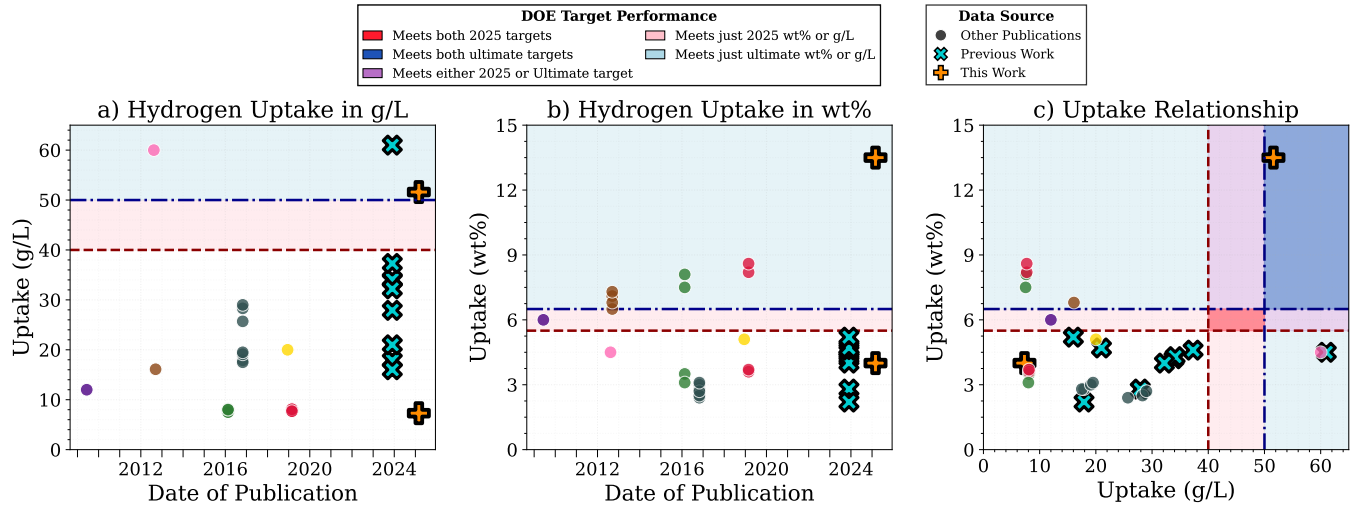


FIG. 1. Leading MOF/COF hydrogen storage performance[11–18] compared to U.S. Department of Energy (DOE) light-duty vehicle (LDV) hydrogen storage targets.[2] Total hydrogen uptakes reported at 298 K and up to 100 bar are shown as: (a) volumetric uptake (g L^{-1}) versus publication year, (b) gravimetric uptake (wt%) versus publication year, and (c) volumetric versus gravimetric uptake, illustrating the trade-off between storage density metrics. In (c), the DOE Ultimate LDV target corresponds to the upper-right quadrant (dark blue). Circles (○) represent literature-reported materials, × denotes our group's prior MSUCOF study, and + indicates results from the present work; identical colors indicate data points originating from the same publication.

vironments within composite materials, thereby modulating catalytic activity for HER/OER reactions.[27] In hypercrosslinked polymers, ferrocene incorporation achieves enhanced H_2 adsorption through a dual mechanism; the abundant micropores provide high surface area, while Fe centers offer strong binding sites via Coulombic Fe– H_2 interactions and favorable spin states [28]. Theoretical studies reveal that low-spin Fe^{2+} centers, as found in ferrocene, can achieve up to a fourfold enhancement in H_2 loading compared to high-spin configurations.[29]

The iron center can engage in direct coordination interactions, while the cyclopentadienyl rings contribute π -electron density for additional binding modes. This dual-site accessibility makes ferrocene an attractive candidate for gas storage applications because it can potentially interact with multiple hydrogen molecules simultaneously without compromising structural integrity.

C. Transition metals in COFs: cost considerations

The incorporation of transition metals into COF structures has been demonstrated to enhance hydrogen storage performance through enhanced adsorbate-framework interactions.[9] However, most successful approaches have relied on expensive precious metals, such as platinum and palladium, limiting practical implementation.[13] Iron-based systems offer a compelling alternative that combines favorable electronic properties with abundant availability and low cost. Iron costs approximately \$0.10 per kg compared to platinum at \$40,000+ per kg, representing a 400,000-fold cost ad-

vantage at the time of writing.

Previous studies have shown that iron-containing binding sites can achieve hydrogen binding energies in the optimal range of 15–25 $\text{kJ}\cdot\text{mol}^{-1}$, sufficient for room-temperature storage while allowing facile desorption.[29] The key advantage of ferrocene over other iron-containing species lies in its exceptional stability and well-defined coordination environment, which should maintain consistent binding properties throughout storage-desorption cycles.

D. Design of MSUCOF-4-FeCp

In the search for a room temperature storage material, researchers often report gravimetric uptake (weight %) up to 100 bar, as this metric prioritizes maximum energy density with minimal added weight; a crucial consideration for transportation applications. The evolution of this field is exemplified in Fig. 1. Early efforts produced materials with exceptional volumetric capacity (Fig. 1 a). The subsequent shift toward prioritizing gravimetric performance has driven exponential improvements among leading MOFs and COFs (Fig. 1 b), yet this optimization often comes at the expense of volumetric performance. This inherent trade-off is illustrated in Fig. 1 c: the most successful materials to date approach either the DOE volumetric or gravimetric target, but not simultaneously both. For example, both taps-COF-1[16] and tapa-COF-1[15] successfully exceed the 6.5 wt% (ultimate gravimetric target) yet achieve less than 20% of the DOE ultimate volumetric target of 50

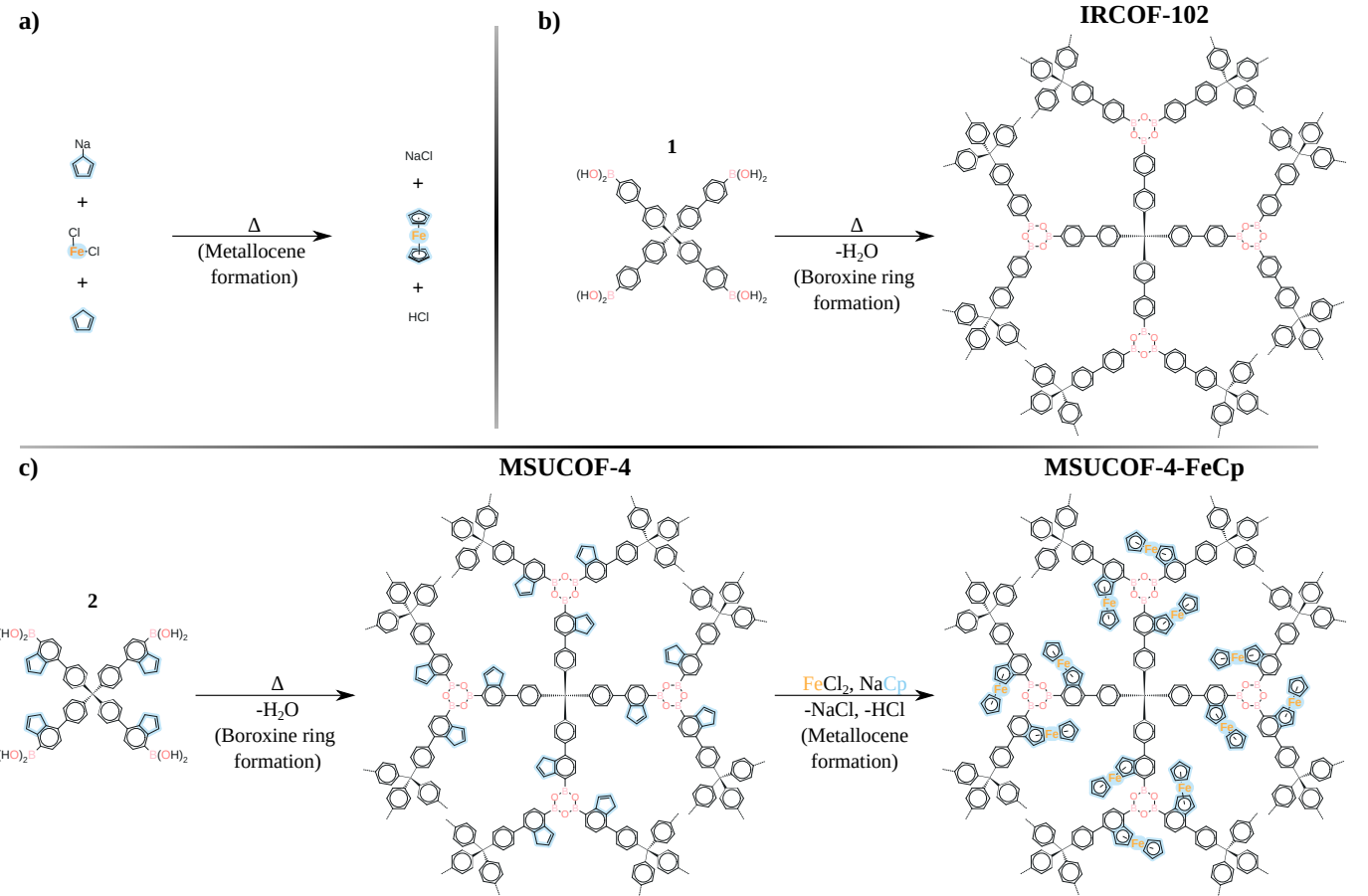


FIG. 2. Schematic illustration of framework synthesis and post-synthetic metallation. (a, top left) Representative metallocene formation reaction, $\text{FeCl} + \text{Cp} + \text{NaCp} \xrightarrow{\Delta} \text{NaCl} + \text{FeCp} + \text{HCl}$. (b, top right) Boroxine condensation of tetrakis(4'-borono-[1,1'-biphenyl]-4-yl)methane (Linker 1) to form IRCOF-102. (c, bottom) Boroxine ring formation of tetrakis(4-(4-boronoinden-7-yl)phenyl)methane (Linker 2) to yield MSUCOF-4, a modified variant of IRCOF-102 in which biphenyl units are replaced by indene moieties; the cyclopentadienyl (Cp) portion of the indene linker is highlighted in light blue. Subsequent post-synthetic metallocene formation affords the metallated framework MSUCOF-4-FeCp. Atom colours: Fe (orange), B (pink), O (red), and C (black).

g/L. Strong binding sites that enhance volumetric capacity typically require heavy metal centers or dense framework designs that penalize gravimetric metrics. Our ferrocene functionalization strategy circumvents this limitation by introducing highly effective binding sites with minimal mass contribution, enabling MSUCOF-4-FeCp to achieve both volumetric and gravimetric targets; a milestone that to the best of our knowledge has not been previously reported for any metal- or covalent-organic framework.

IRCOF-102 was selected as the baseline framework for ferrocene functionalization due to its robust three-dimensional boroxine-linked topology. As an isoreticular extension[30] of COF-102,[31] IRCOF-102 maintains the same tetrahedral node geometry and boroxine chemistry while incorporating extended biphenyl linkers in place of single phenyl units. The framework, constructed from tetrakis(4'-borono-[1,1'-biphenyl]-4-yl)methane (Linker 1), provides larger pores

and higher surface area compared to the parent structure while preserving its synthetic accessibility and structural stability that characterize the COF-102 topology.

Our design strategy employs tetrakis(4-(4-boronoinden-7-yl)phenyl)methane (Linker 2), where the fused cyclopentadienyl ring provides the coordination environment for the formation of ferrocene while the boronic acid at the 4-position enables the condensation of boroxine. This 4,7-substitution maintains a para relationship preserving the linear geometry critical for framework assembly. The framework is designated MSUCOF-4-FeCp instead of MSUCOF-4-FeCp₂ as a Cp ring is integrated within Linker 2, with only the second Cp ring and the Fe center added post-synthetically.

Ferrocene units are located within tritopic pore regions, where three framework struts converge around each boroxine linkage (Fig. 2). These tritopic arrangements create cooperative binding environments that enhance binding energies without reaching

chemisorption,[18] with ferrocene moieties providing multiple binding sites (Fe centers and Cp rings) for complementary hydrogen interactions.

The preferred synthetic route involves the condensation of Linker 2 to form MSUCOF-4, followed by post-synthetic metallation with FeCl_2 and NaCp to produce MSUCOF-4-FeCp. This approach enables comprehensive characterization before metallation and avoids the potential coordination of iron with boroxine-forming groups during synthesis. The transformation proceeds through the deprotonation of the cyclopentadiene ring already in MSUCOF-4 to generate Cp^- , which coordinates with Fe^{2+} and an additional Cp^- (from NaCp) to form the ferrocene unit without sterically hindering pore accessibility. The post-synthetic strategy offers superior control over both framework formation and metal incorporation, consistent with successful metallation protocols in related COF systems.[32]

II. COMPUTATIONAL METHODS

A. Quantum mechanical calculations

Density functional theory (DFT) calculations were performed to determine the electronic structure, binding properties, and optimal geometries of ferrocene-functionalized fragments and the complete MSUCOF-4-FeCp framework.

1. Fragment calculations for force field development

Fragment calculations were performed using CRYSTAL23[33, 34] with the M06 functional[35] and the pob-TZVP-rev2 basis set[36] employing spin-polarized treatment with an extra-large integration grid.[37] The M06 functional was selected for its balanced performance in reproducing thermochemistry and non-covalent interactions.[38] Geometry optimizations employed convergence criteria of 2.72×10^{-11} eV for SCF energy, 1.54×10^{-3} eV \AA^{-1} for RMS forces, and 6.35×10^{-5} \AA for maximum atomic displacements, with Γ -point only Monkhorst-Pack sampling of the 500 \AA supercell.

2. Periodic framework calculations

Full periodic calculations used CRYSTAL23 with HSE06-D3[39–41] providing accurate treatment of electronic properties such as band gap, band structure, and density of states.[42] Comprehensive geometric optimizations for atomic positions and lattice parameters used identical convergence criteria as II A 1 with Monkhorst-Pack Γ -centered grids. Notably, ferrocene units adopt eclipsed Cp conformations within the framework, contrary to the staggered preference of isolated molecules,

because of spatial constraints and electronic interactions with neighboring struts. This eclipsed geometry was maintained in all force field parameterizations fitting.

B. Force field development and validation

Quantum mechanics-derived force fields were developed following our previous methodology[18] employing a Morse potential (Equation 1) for H_2 -ferrocene interactions:

$$U_{ij}^{\text{Morse}}(r_{ij}) = D_0[(1 - e^{-\alpha(r_{ij} - r_0)})^2 - 1] \quad (1)$$

The parameters (D_0 , α , r_0) were fitted to DFT binding energy curves using GULP,[43] sampling multiple Hydrogen configurations (Hc) around eclipsed and staggered variants of ferrocene. A least-squares fitting procedure achieved mean absolute errors below 0.5 $\text{kJ}\cdot\text{mol}^{-1}$ for test configurations (Fig. 3).

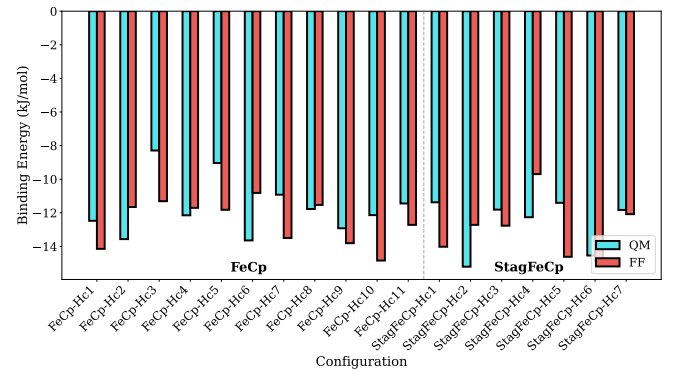


FIG. 3. Validation of the QM-fitted force field for ferrocene– H_2 interactions. Hc denotes hydrogen configuration number. FeCp labels correspond to eclipsed ferrocene (as observed in MSUCOF-4-FeCp), while stagFeCp denotes staggered conformers.

Interaction	D_0 ($\text{kcal}\cdot\text{mol}^{-1}$)	α (\AA^{-1})	r_0 (\AA)
$\text{H}_2\text{-C}$	0.101	1.924	3.120
$\text{H}_2\text{-H}$	0.001	1.849	3.247
$\text{H}_2\text{-Fe}$	1.987	0.466	2.476

TABLE I. Morse potential parameters for H_2 -ferrocene interactions derived from DFT calculations.

The optimized parameters shown in Table I reveal distinctive binding characteristics for the ferrocene iron center. The $\text{H}_2\text{-Fe}$ interaction exhibits a notably deep potential well ($D_0 = 1.987 \text{ kcal}\cdot\text{mol}^{-1}$) combined with a small width parameter ($\alpha = 0.466 \text{ \AA}^{-1}$), indicating diffuse and extended interaction. This combination produces a broad, attractive potential that facilitates hydrogen capture while maintaining reversibility. In contrast, the chelation complex FeCl_2 of our prior study exhibited drastically different electronic environment (D_0

$= 1.092 \text{ kcal}\cdot\text{mol}^{-1}$, $\alpha = 1.180 \text{ \AA}^{-1}$, $r_0 = 3.155 \text{ \AA}$), with weaker, shorter-range binding despite greater metal accessibility.[18] Notably the cyclopentadienyl rings geometrically constrain the Fe center of ferrocene, yet dominate substantial π -electron density which, in addition to its low spin electronic configuration, creates an electron-rich environment that strengthens Coulombic interaction with the H_2 quadrupole moment.

C. Grand Canonical Monte Carlo simulations

Hydrogen storage isotherms were calculated using Grand Canonical Monte Carlo (GCMC) simulations implemented in Materials Studio[44] at 298 K and 1–700 bar. The Metropolis algorithm used translation, rotation, insertion, deletion, and regrowth moves in a 2:1:1:1:0.1 ratio. Equilibrium was achieved after 1,000,000 steps, followed by 3,000,000 production steps to average uptake and isosteric heat of the ensemble (Q_{st}).

D. Equation of state

To convert between fugacity (used in GCMC simulations) and pressure (for experimental comparison), the van der Waals equation of state was employed:[45]

$$\ln \frac{f}{P} = \left(b - \frac{a}{RT} \right) \frac{P}{RT} \quad (2)$$

where f is the fugacity, P is the pressure, T is the temperature (298 K), R is the gas constant, and $a = 0.2476 \text{ L}^2 \text{ bar mol}^{-2}$ and $b = 0.02661 \text{ L mol}^{-1}$ are empirical parameters for hydrogen. In our previous work, we showed that this formulation showed only 0.735% difference from Peng-Robinson at 700 bar.[18]

III. RESULTS AND DISCUSSION

A. Structural properties and design validation

Incorporation of ferrocene into the IRCOF-102 framework results in MSUCOF-4-FeCp, which has well-defined structural properties that support high hydrogen storage performance. As shown in Table II, MSUCOF-4-FeCp maintains a high surface area of $4780 \text{ m}^2 \text{ g}^{-1}$ while achieving a balanced pore volume of $2.55 \text{ cm}^3 \text{ g}^{-1}$ and a void fraction of 0.84. The framework density of 0.12 g cm^{-3} is significantly lower than the previous metal-functionalized variants, contributing to enhanced gravimetric performance. For comparison, structural and uptake results for MSUCOF-(1-3) from our previous work[18] are included.

Pristine COFs often suffer from poor binding energies at room-temperature. Strategies to address this limitation include functionalization, such as incorporating fer-

TABLE II. Comparison of geometric properties of selected MSUCOFs

COF name	Surface area ($\text{m}^2 \text{ g}^{-1}$)	Pore volume ($\text{cm}^3 \text{ g}^{-1}$)	Void fraction	Density (g cm^{-3})
MSUCOF-1	5060	5.06	0.91	0.07
MSUCOF-1-PtCl	2890	2.09	0.88	0.15
MSUCOF-3-CoCl	3770	0.94	0.73	0.28
MSUCOF-3-PtCl	2190	0.55	0.72	0.47
IRCOF-102	5680	5.11	0.90	0.06
MSUCOF-4	4840	4.14	0.88	0.08
MSUCOF-4-FeCp	4780	2.55	0.84	0.12

rocene onto the ligands. Not only does this strategy inject strong binding sites throughout the pore, it does so without an excessive binding strength that can compromise the deliverable capacity (see Section III D).

It is important to note that MSUCOF-4 incorporates one cyclopentadienyl ring as an extended variant of the linkers present in IRCOF-102, yet it lacks the complete $\text{Fe}(\eta^5\text{-C}_5\text{H}_5)$ moiety found in MSUCOF-4-FeCp. This partial functionalization accounts for the intermediate geometric properties observed: MSUCOF-4 shows reduced surface area (4840 vs $5680 \text{ m}^2 \text{ g}^{-1}$), pore volume (4.14 vs $5.11 \text{ cm}^3 \text{ g}^{-1}$), and void fraction (0.88 vs 0.90) compared to pristine IRCOF-102. However, as shown in subsequent sections, MSUCOF-4 still exhibits hydrogen storage performance comparable to IRCOF-102 despite these geometric differences. This indicates that the exceptional performance of MSUCOF-4-FeCp is primarily due to the ferrocene complex-hydrogen interactions rather than purely geometric factors.

B. Electronic structure calculations

The electronic properties of the pristine IRCOF-102 and functionalized MSUCOF-4-FeCp were studied and visualized by calculating the band structure and the density of states (Fig. 4). For these calculations, we follow the methods described in Section II A 2. These calculations were performed using spin unrestricted DFT, allowing α and β orbitals to vary to capture any potential magnetic ordering. These MSUCOF-4 and IRCOF-102 families of materials follow the $\Gamma\text{-}\bar{4}3d$ space group (No. 220); accordingly the reciprocal space was sampled in the high symmetry path $\Gamma\text{-H-N-}\Gamma\text{-P-H|P-N}$ as determined by SeeKPath to capture the relevant band dispersion.[46] The atom-projected density of states will reveal the atomic contributions at frontier bands.

These results show expected trends for porous materials. In both materials, many of the bands exhibit minimal band dispersion (flat bands with no spin asymmetry), indicative of localized molecular orbitals throughout the organic linkages. Additionally, IRCOF-102 displays a band gap large enough to classify it as an insulator ($E_g = 4.10 \text{ eV}$), which is consistent with its composition of light main-group elements (C, B, O) engaged in

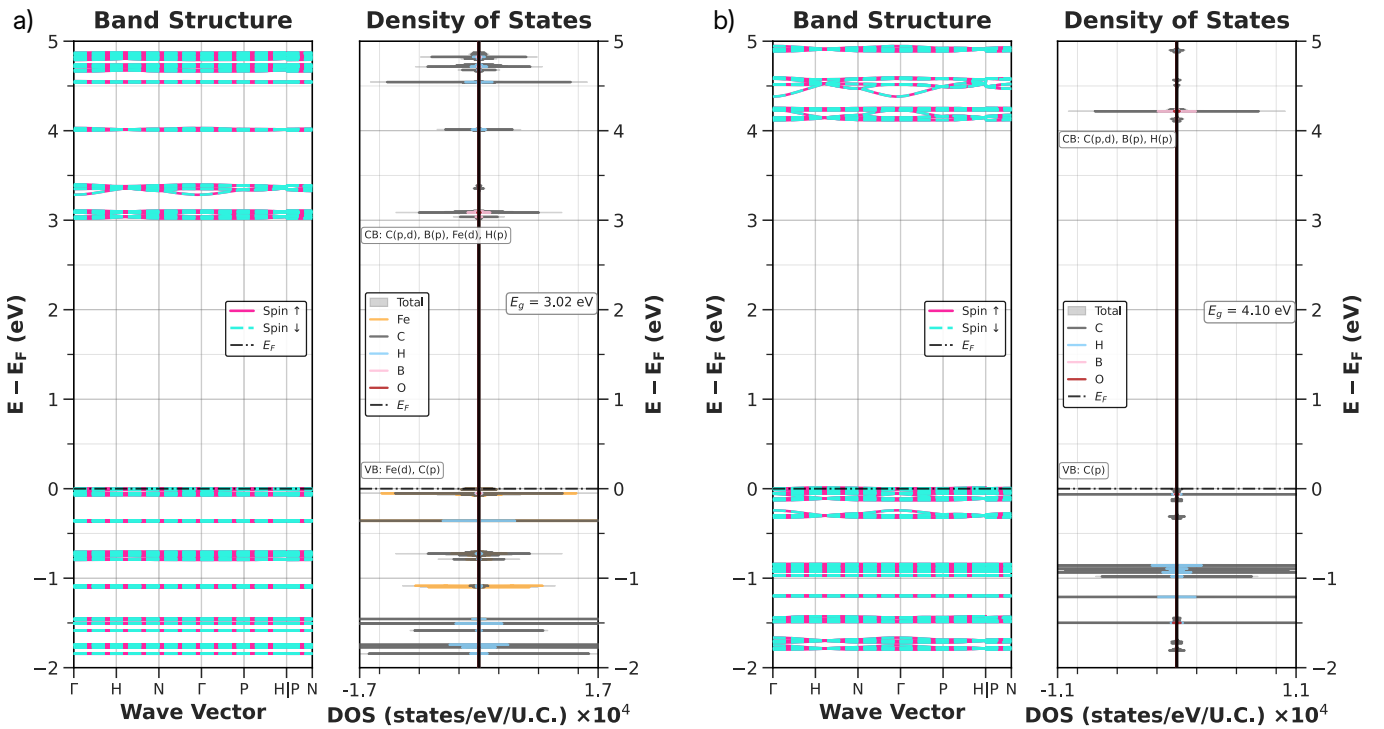


FIG. 4. Electronic structure of (a) MSUCOF-4-FeCp and (b) IRCOF-102, showing band structure (left) and density of states (right). Both materials exhibit flat bands typical of porous materials. Functionalization in MSUCOF-4-FeCp narrows the band gap, enhancing the potential for electronic or catalytic applications.

saturated covalent bonding. MSUCOF-4-FeCp acts as a functionalized variant with $\text{Fe}(\eta^5\text{-C}_5\text{H}_5)_2$ additions in tritopic regions within the pore. By adding this moiety, MSUCOF-4-FeCp experiences a more narrow band gap of $E_g = 3.02$ eV (notably 410 nm in the visible light range), enhancing its potential for electronic and catalytic applications.

Analysis of the HOMO and LUMO character of MSUCOF-4-FeCp reveals that the valence band edge is predominantly Fe-centered, with contributions from Fe(d) and C(p) orbitals of the cyclopentadienyl rings. Meanwhile, the conduction band edge is localized on an organic framework, primarily C(p,d), with minor contributions from B(p), Fe(d), and H(p). This spatial separation of frontier orbitals is indicative of metal-to-ligand charge transfer, suggesting that photoexcitation would generate oxidized Fe centers and reduced organic sites. These charge-separated states are favorable for both photocatalysis and electrocatalysis, as is common with ferrocene-based systems. The flat bands reflect the localized nature of these redox-active sites, which is typical of molecular catalysts embedded in porous frameworks and does not preclude efficient catalysis where electron transfer could occur at discrete metal centers rather than in a band-like transport.

C. Hydrogen storage performance

The hydrogen storage performance of MSUCOF-4-FeCp demonstrates exceptional promise in meeting DOE targets. Fig. 5 presents both gravimetric and volumetric uptake isotherms at 298 K, showing that MSUCOF-4-FeCp achieves 18.0 wt% hydrogen uptake and 72.6 g H₂ L⁻¹ at 700 bar. This performance represents a significant improvement over the parent IRCOF-102, and the gravimetric uptake is approximately 3.5 times higher than that of the denser MSUCOF-3-PtCl variant. We chose to measure up to these pressures as existing commercial hydrogen fuel cell vehicles are already available to the market offering pressure tanks up to 700 bar.

Working capacity (WC)—defined as the amount of hydrogen that can be practically delivered between high storage pressure (700 bar) and rough delivery pressure (5 bar)—is a critical heuristic to approximate realistic delivery that can be obtained in a reasonable time frame. Unlike MSUCOF-3-PtCl, which detrimentally locks hydrogen even at low pressures, MSUCOF-4-FeCp maintains a balanced adsorption profile that ensures higher usable capacity under working conditions.

The log-log total uptake plots (Fig. 5 a,c) best capture low pressure adsorption behavior, where the linear response reflects the Henry regime in which uptake scales proportionally with pressure. Sub-linear behavior develops as saturation effects emerge, ultimately reaching a plateau that is characteristic of Langmuir-like saturation.

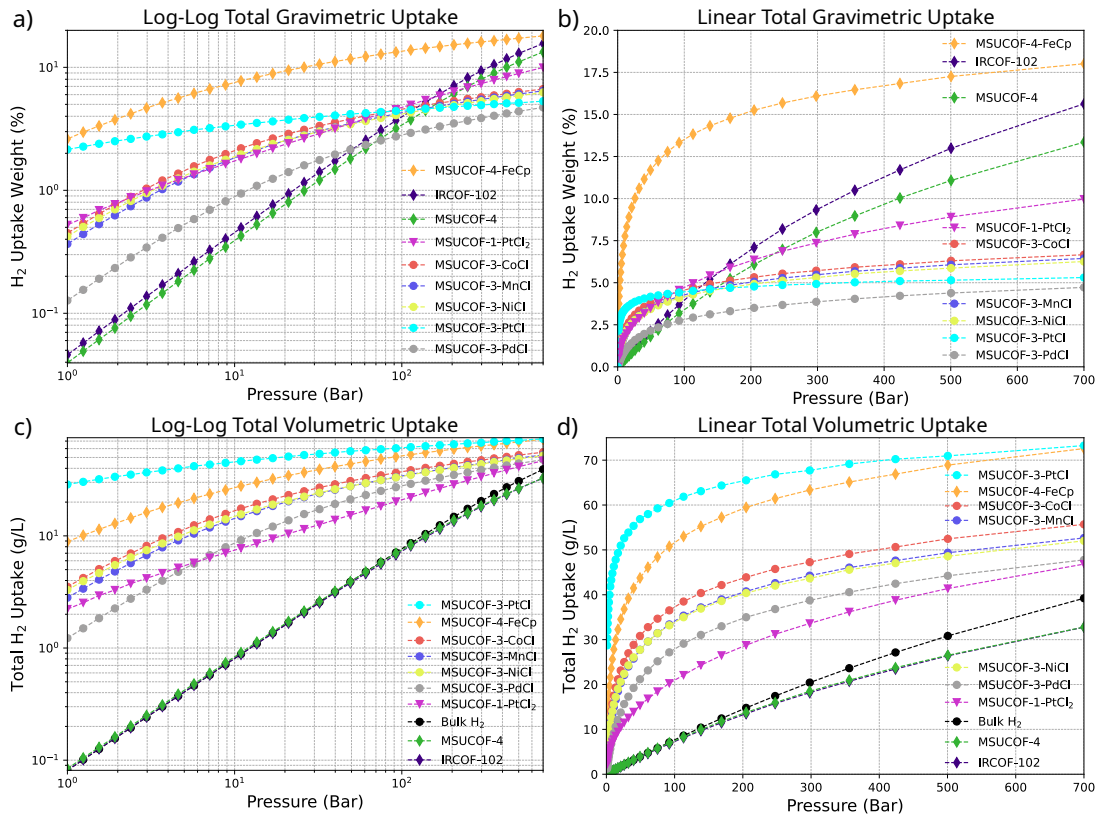


FIG. 5. Comparison of total gravimetric (a,b) and volumetric (c,d) uptake at 298 K for the MSUCOF-4 family against top-performing MSUCOF variants. Log-log plots (a,c) provide detail in the low-pressure region, while linear plots (b,d) show high-pressure behavior. MSUCOF-4-FeCp demonstrates superior performance across all pressure ranges.

In contrast, the linear plots (Fig. 5 b,d) better resolve high pressure behavior. These complementary representations reveal distinct material characteristics: strong adsorbents such as MSUCOF-3-PtCl dominate at low pressure, but also saturate earlier.

In terms of volumetric uptake (Fig. 5 b), MSUCOF-4-FeCp retains less H_2 at low pressures than MSUCOF-3-PtCl₂, but still more than the first-row transition metal (TM) chelation complexes of MSUCOF-3-TMCl₂. However, the linear volumetric uptake plot (Fig. 5 d) reveals that MSUCOF-4-FeCp approaches the energy density of MSUCOF-3-PtCl₂ at high pressures. This balance is critical for volumetric working capacities (WC_v): MSUCOF-4-FeCp achieves 52.2 $\text{g H}_2 \text{ L}^{-1}$, surpassing all previous variants of MSUCOF-1-3 (32.6–44.3 $\text{g H}_2 \text{ L}^{-1}$) by accumulating substantial H_2 at high pressures without detrimentally locking it in low pressures. Despite its exceptional total volumetric uptake, MSUCOF-3-PtCl₂ hinders its own WC_v to 32.6 $\text{g H}_2 \text{ L}^{-1}$ precisely for this reason.

The spacious unit cell inherited from IRCOF-102 (roughly 4× the volume of MSUCOF-3) reduces the density of the framework, allowing MSUCOF-4-FeCp to achieve its high volumetric performance without sacrificing its gravimetric uptake. Gravimetric uptake increases from 2.6 wt% at 1 bar to 18.0 wt% at 700 bar, yielding

a gravimetric working capacity (WC_g) of 12.2 wt%. The low-density MSUCOF-2 family achieves 11.4–18.9 wt% WC_g but suffers from poor volumetric performance (33.2–38.7 $\text{g H}_2 \text{ L}^{-1}$), while the pristine IRCOF-102 (15.4 wt%, 32.4 $\text{g H}_2 \text{ L}^{-1}$) closely matches the pristine MSUCOF-1 (15.2 wt%, 32.4 $\text{g H}_2 \text{ L}^{-1}$). Thus, MSUCOF-4-FeCp is one of the only materials capable of simultaneously satisfying both DOE ultimate targets: 6.5 wt% gravimetric capacity and 50 $\text{g H}_2 \text{ L}^{-1}$ volumetric capacity.

The net uptake metric provides another crucial performance indicator by comparing the porous material with compressed bulk hydrogen under identical conditions. Positive net uptake values indicate that the incorporation of the porous material provides a storage advantage over simple compression, while negative values suggest that the added weight and volume of the material actually reduce overall storage efficiency. The net uptake plot (Fig. 6) reveals peaks at optimal pressures (P_{opt}) that reflect the interplay between binding strength and saturation behavior. MSUCOF-4-FeCp achieves $P_{\text{opt}} = 145$ bar; substantially higher than MSUCOF-3-PtCl ($P_{\text{opt}} = 65$ bar), which saturates prematurely due to its stronger binding and smaller pores, yet comparable to the dense first-row transition metal variants of MSUCOF-3 ($P_{\text{opt}} \approx 130$ –139 bar). Crucially, MSUCOF-4-FeCp maintains positive net uptake across a broad pressure range, vali-

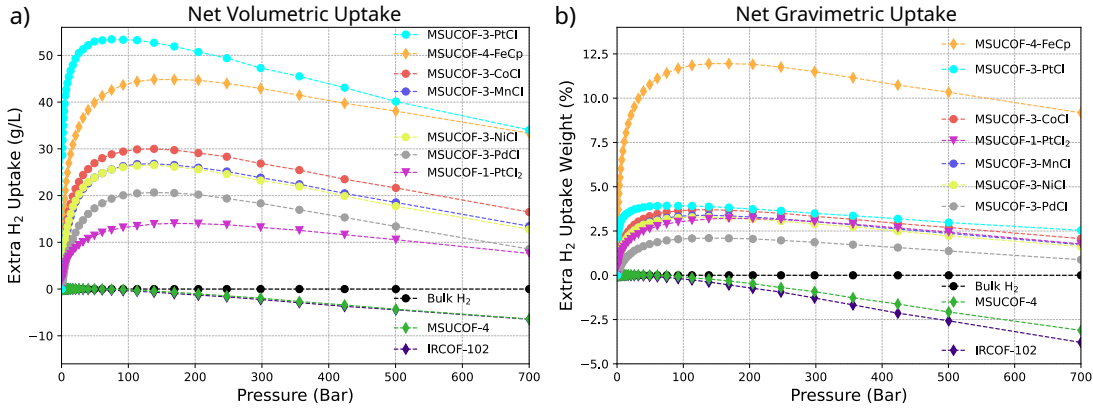


FIG. 6. High-pressure H₂ net volumetric and gravimetric isotherms showing deliverable capacity advantages of MSUCOF-4-FeCp compared to other variants at 298 K.

dating that the enhanced ferrocene binding interactions more than compensate for the framework's mass and volume even at 700 bar. These metrics are summarized in Table III. Based on this usable working capacity, several variants of MSUCOF achieve either the 2025 DOE gravimetric or volumetric target, but MSUCOF-4-FeCp is still the only material that simultaneously satisfies both ultimate targets (6.5 wt% and 50 g H₂ L⁻¹).

TABLE III. Working capacity performance metrics for select MSUCOF variants at 298 K. P_{opt} denotes the optimal pressure at which net uptake is maximized, WC_g and WC_v represent gravimetric and volumetric working capacities (700 bar to 5 bar), respectively.

Material	P_{opt}	WC _g	WC _v
	(bar)	(wt%)	(g H ₂ L ⁻¹)
MSUCOF-1-PtCl ₂	169	8.71	41.4
MSUCOF-3-CoCl	139	5.22	44.3
MSUCOF-3-MnCl	139	5.20	43.1
MSUCOF-3-NiCl	130	4.95	41.7
MSUCOF-3-PdCl	139	4.20	42.7
MSUCOF-3-PtCl	75	2.29	32.6
IRCOF-102	3	15.4	32.4
MSUCOF-4	26	13.2	32.8
MSUCOF-4-FeCp	145	12.2	52.2
<i>DOE Targets</i>			
2025	—	5.5	40.0
Ultimate	—	6.5	50.0

D. Binding energy analysis and mechanisms

Analysis of isosteric heat of adsorption (Q_{st}) demonstrates that MSUCOF-4-FeCp achieves optimal binding energies within the intermediate physisorption regime (Fig. 7). Interestingly, the binding energy profile is similar to that of MSUCOF-3-CoCl, a material that we previously recognized for its superior working capacity. Moderate binding strengths (7–20 kJ·mol⁻¹) allow efficient hydrogen adsorption at high pressures without locking hydrogen into the structure.

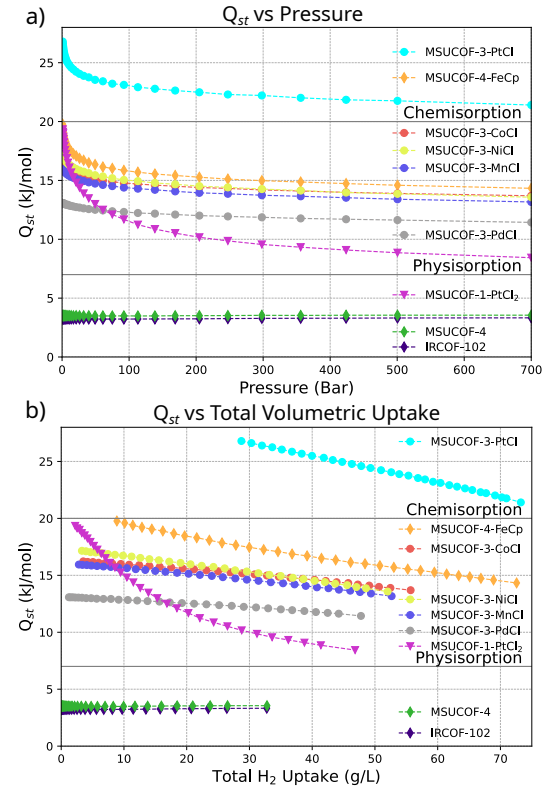


FIG. 7. High-pressure H₂ isosteric heat of adsorption (Q_{st}) at 298 K versus (a) Pressure and (b) total H₂ uptake, showing optimal binding energy characteristics for MSUCOF-4-FeCp, which lies entirely between chemi- and physisorption for H₂.

From the GCMC simulations, we can derive a probability distribution $P(E)$ that illustrates the proportions of adsorbed H₂ molecules experiencing interaction energy E at thermodynamic equilibrium. This distribution satisfies the normalization condition:

$$\int_{-\infty}^{\infty} P(E) dE = 1 \quad (3)$$

In Equation 3, the negative integration limits are associated with energies that correspond to attractive interactions, while any interaction greater than zero is repulsive. The isosteric heat of adsorption is directly tied to the ensemble-averaged interaction energy through:

$$Q_{\text{st}} = -\langle E \rangle = - \int_{-\infty}^{\infty} E \cdot P(E) dE \quad (4)$$

This relationship (Equation 4) shows that Q_{st} represents the mean of the energy distribution. Note the negative sign that converts the interaction energy to a positive heat of adsorption, following the standard reporting convention. Then it follows that the variance of the distribution can be calculated with the following.

$$\sigma^2 = \int_{-\infty}^{\infty} (E - \langle E \rangle)^2 \cdot P(E) dE \quad (5)$$

Equation 5 quantifies the diversity of binding sites within the framework. A larger variance indicates a broader range of binding environments, which can be advantageous for maintaining adsorption across various pressure levels.

The analysis of the energy distribution shed light on the binding mechanisms within select MSUCOFs (Fig. 8). At 1 bar, the distribution shows a primary broad peak with a long tail towards 0, indicating that the majority of initial interactions occur at favorable primary binding sites, while few stragglers permeate the pore and interact at weaker sites. At higher pressures, there is a clear right shift of both the overall average binding strength (Q_{st}) and the average of each individual site (μ_i) as they begin to saturate. When secondary peaks appear as shoulders on the primary distribution, accurate quantification requires a method to de-convolute the isolated individual contributions. Each peak i is fitted with an asymmetric (skewed) Gaussian function:

$$P_i(E) = \begin{cases} A_i \exp\left(-\frac{(E-\mu_i)^2}{2\sigma_{L,i}^2}\right) & \text{for } E \leq \mu_i \\ A_i \exp\left(-\frac{(E-\mu_i)^2}{2\sigma_{R,i}^2}\right) & \text{for } E > \mu_i \end{cases} \quad (6)$$

where A_i is the amplitude, μ_i is the center (mean energy), and $\sigma_{L,i}$ and $\sigma_{R,i}$ are the widths left and right, respectively. This asymmetric form captures the characteristic skewness of the interaction energy distributions. All peaks are fitted simultaneously using a composite model to avoid double-counting in overlapping regions while preserving an accurate determination of individual binding site energies. In Equation 7, N is the number of peaks and all parameters.

$$P(E) = \sum_{i=1}^N P_i(E) \quad (7)$$

The average energy for each de-convoluted peak is given by its fitted Gaussian mean μ_i :

$$\langle E \rangle_{\text{peak},i} = \mu_i \quad (8)$$

This approach provides site-specific energies that are more accurate than simple numerical integration over peak boundaries, which can be biased by overlapping contributions from adjacent peaks. The fraction of H_2 molecules that experience energies within the peak i is shown in Equation 9. The individual Gaussian component $P_i(E)$ is integrated throughout the energy range and normalized by the total area under $P(E)$ to determine the fraction of molecules that experience that particular binding mode.

$$f_{\text{peak},i} = \frac{\int_{-\infty}^{\infty} P_i(E) dE}{\int_{-\infty}^{\infty} P(E) dE} \quad (9)$$

At 1 bar, the main peak for MSUCOF-4-FeCp, which is centered around $-18.8 \text{ kJ}\cdot\text{mol}^{-1}$ ($-4.5 \text{ kcal}\cdot\text{mol}^{-1}$), highlights the dominant $\text{Fe}-\text{H}_2$ interaction. Any unusual features at weaker binding energies likely stem from any of the following: geometries that are sterically constrained; shielded H_2-H_2 interactions; compounded effects at key overlapped regimes amongst tritopic regions; or interactions with the cyclopentadienyl rings.

When pressure increases to 700 bar, the distribution shows two distinct peaks at -13.2 and $-7.7 \text{ kJ}\cdot\text{mol}^{-1}$ (-3.2 and $-1.8 \text{ kcal}\cdot\text{mol}^{-1}$), which relate to different binding environments within the ferrocene coordination sphere. The predominant broad peak at $-13.2 \text{ kJ}\cdot\text{mol}^{-1}$ likely corresponds to coordination with the low-spin Fe^{2+} center in ferrocene, which theoretical studies have shown provides enhanced H_2 binding compared to high-spin configurations.[29] Likewise, the sharp peak at $-7.7 \text{ kJ}\cdot\text{mol}^{-1}$ can be partially attributed to previously mentioned weaker binding regimes that serve as a backup when the primary binding modes saturate.

As pressure evolves, $P(E)$ shows a sequential occupation of binding sites based on their relative affinities. At low pressures, mainly the strongest sites (leftmost region of $P(E)$) are populated, resulting in higher average binding energies. As pressure increases and strong sites saturate, weaker sites begin to dominate, shifting the distribution toward less negative energies and reducing the ensemble-averaged Q_{st} .

From the definition of $Q_{\text{st}} = -\langle E \rangle$ in Equation 4, the response of the binding energy upon loading follows directly:

$$\frac{\partial Q_{\text{st}}}{\partial n} = -\frac{\partial \langle E \rangle}{\partial n} \quad (10)$$

where n represents the hydrogen load. For heterogeneous adsorbents possessing a distribution of binding site energies, adsorption should proceed sequentially: the

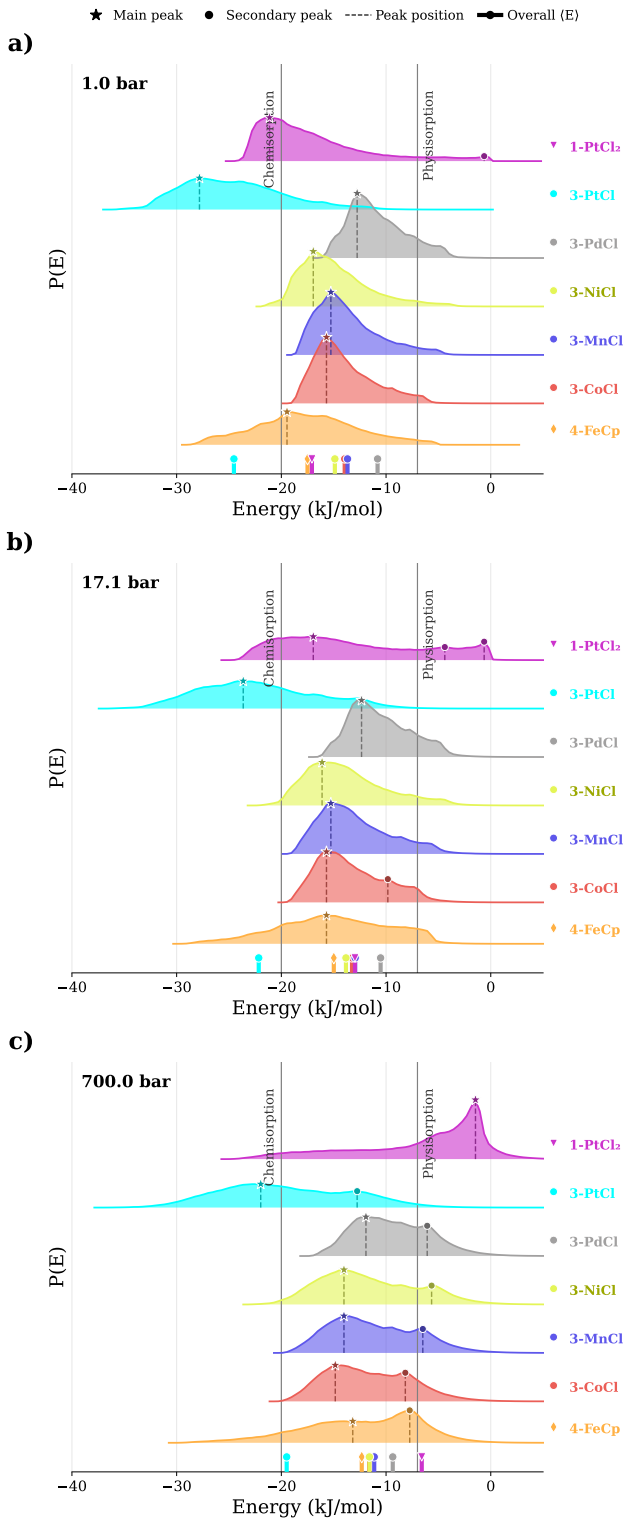


FIG. 8. Ridge plot of H_2 interaction energy distributions $P(E)$ at (a) 1, (b) 17.1, and (c) 700 bar; curves are vertically offset for clarity. Solid stars and open circles mark primary and secondary Q_{st} peaks, respectively. Colored ticks indicate ensemble-averaged energies $\langle E \rangle$; vertical dashed lines delineate chemisorption ($>20 \text{ kJ}\cdot\text{mol}^{-1}$) and physisorption ($<7 \text{ kJ}\cdot\text{mol}^{-1}$) regimes.

strongest sites populate first, followed by progressively weaker sites as loading increases. Consequently, $\langle E \rangle$ shifts towards less negative values with increasing n . In contrast, homogeneous adsorbents with uniform binding sites remain constant regardless of loading.

$$\frac{\partial Q_{\text{st}}}{\partial n} \begin{cases} < 0 & \text{(heterogeneous)} \\ \approx 0 & \text{(homogeneous)} \end{cases} \quad (11)$$

This negative slope is characteristic of heterogeneous adsorbents and is observed for the most promising MSUCOF materials in Fig. 7 b. MSUCOF-4-FeCp maintains a constant negative slope across a wide range of uptakes/loading, which indicates that it maintains a distribution of binding sites rather than uniform interactions. In contrast, MSUCOF-4 and IRCOF-102 are flat, suggesting that H_2 is mainly bulk filling within the pores. MSUCOF-1-PtCl₂ is an interesting case where beyond 15 g $\text{H}_2 \text{ L}^{-1}$ it quickly flattens as it approaches saturation.

TABLE IV. Energy distribution statistics for hydrogen adsorption derived from GCMC simulations at 298 K. N denotes the number of resolved peaks.

Material	P bar	$\langle E \rangle$ $\text{kJ}\cdot\text{mol}^{-1}$	Q_{st} $\text{kJ}\cdot\text{mol}^{-1}$	σ $\text{kJ}\cdot\text{mol}^{-1}$	Peaks N
<i>Low pressure</i>					
MSUCOF-1-PtCl ₂	1	-17.08	17.08	5.18	2
MSUCOF-3-CoCl	1	-13.96	13.96	2.89	1
MSUCOF-3-MnCl	1	-13.68	13.68	3.02	1
MSUCOF-3-NiCl	1	-14.89	14.89	3.36	1
MSUCOF-3-PdCl	1	-10.81	10.81	2.74	1
MSUCOF-3-PtCl	1	-24.53	24.53	4.81	1
MSUCOF-4-FeCp	1	-17.51	17.51	4.79	1
<i>Intermediate pressure</i>					
MSUCOF-1-PtCl ₂	17.1	-12.97	12.97	6.68	3
MSUCOF-3-CoCl	17.1	-13.25	13.25	3.28	2
MSUCOF-3-MnCl	17.1	-12.95	12.95	3.39	1
MSUCOF-3-NiCl	17.1	-13.83	13.83	3.78	1
MSUCOF-3-PdCl	17.1	-10.52	10.52	2.91	1
MSUCOF-3-PtCl	17.1	-22.16	22.16	5.58	1
MSUCOF-4-FeCp	17.1	-14.99	14.99	5.20	1
<i>High pressure</i>					
MSUCOF-1-PtCl ₂	700	-6.59	6.59	6.15	1
MSUCOF-3-CoCl	700	-11.62	11.62	3.98	2
MSUCOF-3-MnCl	700	-11.13	11.13	4.13	2
MSUCOF-3-NiCl	700	-11.60	11.60	4.63	2
MSUCOF-3-PdCl	700	-9.36	9.36	3.55	2
MSUCOF-3-PtCl	700	-19.49	19.49	6.16	2
MSUCOF-4-FeCp	700	-12.32	12.32	5.52	2

A summary breakdown of the values and statistics in Fig. 8 is shown in Table IV (a more detailed breakdown can be found in Table S1). The dual-peak behavior at high pressures supports the idea of a multi-binding site mechanism, which is key to the exceptional storage capacity of MSUCOF-4-FeCp. Integration of individual peaks reveals that the majority (83%) of adsorbed H_2

still interact with Fe centers at 700 bar, while the remaining fraction (17%) engages with weaker framework sites. This strong preference for metal coordination demonstrates the critical role of ferrocene centers in achieving high storage densities. In the case of MSUCOF-1-PtCl₂, up to three peaks are observed: one, primary binding site; two, secondary or shielded binding sites; and three, a bulk filled interaction near 0 kJ·mol⁻¹ as the previous two saturate.

E. Practical considerations

Beyond the cost advantages mentioned earlier (Section IC), ferrocene functionalization brings additional practical benefits for large-scale implementation. Iron is among the most abundant elements in the Earth's crust, with global reserves exceeding 800 billion metric tonnes of crude ore, while platinum-group metals are scarce and geographically concentrated, with production dominated by South Africa and Russia.[47] This abundance makes iron-based systems less susceptible to supply chain disruptions and price volatility that affect precious metal-dependent technologies.

MSUCOF-4-FeCp outperforms both pristine COFs and other metal-functionalized variants, while offering significant economic and strategic benefits. The gravimetric uptake of 18.0 wt% significantly exceeds the DOE target of 6.5 wt%, while the volumetric uptake of 72.6 g H₂ L⁻¹ exceeds the target of 50 g H₂ L⁻¹. More importantly, balanced performance metrics ensure high deliverable capacity under practical operating conditions.

The stable and well-defined nature of ferrocene, along with its demonstrated thermal stability up to 400°C, suggests excellent cycling stability for pressure swing adsorption applications. It should be noted that these computational results represent idealized conditions: perfect crystallinity without defects, vacancies, or residual solvent molecules; experimental performance may deviate accordingly. Thus, experimental synthesis, optimization, and long-term performance validation are essential for future work.

CONCLUSIONS

We have demonstrated through comprehensive first-principles multiscale computational simulations that ferrocene-functionalized covalent organic frameworks represent a promising new class of hydrogen storage materials. MSUCOF-4-FeCp achieves exceptional performance metrics with 18.0 wt% gravimetric and 72.6 g H₂ L⁻¹ volumetric hydrogen uptake at 298 K and 700 bar, substantially exceeding DOE targets. More critically, the working capacities of 12.2 wt% (WC_g) and 52.2 g H₂ L⁻¹ (WC_v) demonstrate that MSUCOF-4-FeCp is, to our knowledge, the only porous framework material to

simultaneously satisfy both DOE ultimate targets under practical operating conditions.

Energy distribution analysis from GCMC simulations reveals that iron coordination, the cyclopentadienyl ring, and tritopic region compounded interactions provide multiple hydrogen binding sites while maintaining moderate binding energies. This approach offers significant economic advantages over precious metal alternatives while achieving exceptional performance. The stable and well-defined nature of ferrocene suggests excellent potential for cycling stability and long-term performance.

Ferrocene incorporation narrows the band gap from 4.10 eV to 3.02 eV (410 nm), with the metal-to-ligand charge transfer character creating discrete, localized redox-active sites throughout the framework. These molecular catalytic centers, combined with the porous architecture, suggest applications in photocatalysis and electrocatalysis beyond hydrogen storage.

This work establishes ferrocene functionalization as a viable strategy for enhancing the hydrogen storage performance in COFs and provides a foundation for future experimental validation. The computational framework developed here can be extended to explore other metallocene systems and optimize material properties for specific applications.

SUPPLEMENTARY INFORMATION

Supplementary Information is available: Surface area and pore volume calculations, force field fitting details, excess uptake isotherms, hydrogen density fields, energy distribution peak deconvolution parameters, and optimized crystal structure geometries.

ACKNOWLEDGEMENTS

M.D. and J.L.M.-C. acknowledged partial support from startup funds from Michigan State University. M.D. acknowledges the support from MSU's College of Engineering Graduate Office Fellowship and Dissertation Completion Fellowship. This work was supported in part through computational resources and services provided by the Institute for Cyber-Enabled Research at Michigan State University. M.D. also thanks Daniel Maldonado-Lopez for helpful discussions.

AUTHOR CONTRIBUTIONS

M.D. performed the DFT calculations, validated the force field parameters, performed the GCMC simulations, analyzed the data, created all figures, and wrote the manuscript. J.L.M.-C. conceived the material design, developed the initial methodology and results, supervised the project, co-wrote and revised the manuscript. Both

authors discussed the results and approved the final version.

COMPETING INTERESTS

A patent application related to this work has been filed and is currently pending.

DATA AVAILABILITY

Data and codes supporting the findings of this study are available from the corresponding author on a reasonable request.

[1] U.S. Department of Energy. Hydrogen shot (2021). URL <https://www.energy.gov/eere/fuelcells/hydrogen-shot-summit>.

[2] U.S. Department of Energy. Technical targets for onboard hydrogen storage for light-duty vehicles (2020). URL <https://www.energy.gov/eere/fuelcells/doe-technical-targets-onboard-hydrogen-storage-light-duty-vehicles>.

[3] Yaghi, O. M. Reticular chemistry-construction, properties, and precision reactions of frameworks. *Journal of the American Chemical Society* **138**, 15507–15509 (2016).

[4] Wu, H., Simmons, J. M., Srinivas, G., Zhou, W. & Yildirim, T. Adsorption Sites and Binding Nature of CO₂ in Prototypical Metal-Organic Frameworks: A Combined Neutron Diffraction and First-Principles Study. *The Journal of Physical Chemistry Letters* **1**, 1946–1951 (2010).

[5] Mendoza-Cortés, J. L., Han, S. S., Furukawa, H., Yaghi, O. M. & Goddard III, W. A. Adsorption Mechanism and Uptake of Methane in Covalent Organic Frameworks: Theory and Experiment. *The Journal of Physical Chemistry A* **114**, 10824–10833 (2010).

[6] Fan, W. *et al.* Multivariate Polycrystalline Metal-Organic Framework Membranes for CO₂/CH₄ Separation. *Journal of the American Chemical Society* **143**, 17716–17723 (2021).

[7] Humby, J. D. *et al.* Host-guest selectivity in a series of isoreticular metal-organic frameworks: observation of acetylene-to-alkyne and carbon dioxide-to-amide interactions. *Chemical Science* **10**, 1098–1106 (2019).

[8] Al-Rowaili, F. N. *et al.* A review for Metal-Organic Frameworks (MOFs) utilization in capture and conversion of carbon dioxide into valuable products. *Journal of CO₂ Utilization* **53**, 101715 (2021).

[9] Han, S. S., Mendoza-Cortés, J. L. & Goddard III, W. A. Recent advances on simulation and theory of hydrogen storage in metal-organic frameworks and covalent organic frameworks. *Chemical Society Reviews* **38**, 1460–1476 (2009).

[10] Caskey, S. R., Wong-Foy, A. G. & Matzger, A. J. Dramatic Tuning of Carbon Dioxide Uptake via Metal Substitution in a Coordination Polymer with Cylindrical Pores. *Journal of the American Chemical Society* **130**, 10870–10871 (2008).

[11] Klontzas, E., Tylianakis, E. & Froudakis, G. E. Hydrogen Storage in Lithium-Functionalized 3-d Covalent-Organic Framework Materials. *The Journal of Physical Chemistry C* **113**, 21253–21257 (2009).

[12] Guo, J.-H., Zhang, H., Gong, M. & Cheng, X.-L. Ca²⁺- and Mg²⁺-doped covalent organic frameworks exhibiting high hydrogen and acetylene storage. *Structural Chemistry* **24**, 691–703 (2013).

[13] Mendoza-Cortés, J. L., Goddard III, W. A., Furukawa, H. & Yaghi, O. M. A Covalent Organic Framework that Exceeds the DOE 2015 Volumetric Target for H₂ Uptake at 298 K. *The Journal of Physical Chemistry Letters* **3**, 2671–2675 (2012).

[14] Pramudya, Y. & Mendoza-Cortés, J. L. Design Principles for High H₂ Storage Using Chelation of Abundant Transition Metals in Covalent Organic Frameworks for 0–700 bar at 298 K. *Journal of the American Chemical Society* **138**, 15204–15213 (2016).

[15] Li, X.-D. *et al.* Predicting 1,3,5,7-tetrakis(4-aminophenyl)adamantine based covalent-organic frameworks as hydrogen storage materials. *RSC Advances* **6**, 21517–21525 (2016).

[16] Li, X.-D., Zhang, Y., Guo, J.-H., Yu, S.-Q. & Du, D.-W. Computer-aided prediction of structure and hydrogen storage properties of tetrakis(4-aminophenyl)silsesquioxane based covalent-organic frameworks. *International Journal of Hydrogen Energy* **44**, 8357–8364 (2019).

[17] Ghosh, S. & Singh, J. K. Hydrogen adsorption in pyridine bridged porphyrin-covalent organic framework. *International Journal of Hydrogen Energy* **44**, 1782–1796 (2019).

[18] Djokic, M. & Mendoza-Cortés, J. L. Multi-Binding Sites United in Covalent-Organic Frameworks (MSUCOF) for H₂ Storage and Delivery at Room Temperature. *Energy and Fuels* **38**, 4711–4720 (2024).

[19] Kealy, T. J. & Pauson, P. L. A new type of organo-iron compound. *Nature* **168**, 1039–1040 (1951).

[20] Wilkinson, G., Rosenblum, M., Whiting, M. C. & Woodward, R. B. The structure of iron bis-cyclopentadienyl. *Journal of the American Chemical Society* **74**, 2125–2126 (1952).

[21] Fischer, E. O. & Pfab, W. Cyclopentadienylmetallkomplexe ein neuer typ metallorganischer verbindungen. *Zeitschrift fur Naturforschung - Section B Journal of Chemical Sciences* **7**, 377–379 (1952).

[22] Laszlo, P. & Hoffmann, R. Ferrocene: Ironclad history or rashomon tale? *Angewandte Chemie International Edition* **39**, 123–124 (2000).

[23] Roy, G. *et al.* Ferrocene as an iconic redox marker: From solution chemistry to molecular electronic devices. *Coordination Chemistry Reviews* **473**, 214816 (2022).

[24] Lai, G.-Q., Li, N., He, J. & Lan, Y.-Q. A ferrocene-modified stable metal-organic framework for efficient CO₂ photoreduction reaction. *Chemical Communications* **59**, 12471–12474 (2023).

[25] Samy, M. M. *et al.* Conjugated microporous polymers containing ferrocene units for high carbon dioxide uptake

and energy storage. *Materials Chemistry and Physics* **287**, 126177 (2022).

[26] Chen, Y., Cao, X., Zhu, H. & Liu, Y. Preparation of a porous carbon from ferrocene-loaded polyaniline and its use in hydrogen adsorption. *International Journal of Hydrogen Energy* **37**, 7629–7637 (2012).

[27] Sariga & Varghese, A. The renaissance of ferrocene-based electrocatalysts: Properties, synthesis strategies, and applications. *Topics in Current Chemistry* **381**, 1–93 (2023).

[28] Peng, Q. *et al.* Ferrocene-based hypercrosslinked polymers derived from phenolic polycondensation with unexpected H₂ adsorption capacity. *Materials Today Chemistry* **24**, 100854 (2022).

[29] Cha, M. H., Nguyen, M. C., Lee, Y. L., Im, J. & Ihm, J. Iron-decorated, functionalized metal organic framework for high-capacity hydrogen storage: First-principles calculations. *Journal of Physical Chemistry C* **114**, 14276–14280 (2010).

[30] Nguyen, H. L. Reticular design and crystal structure determination of covalent organic frameworks. *Chemical Science* **12**, 8632–8647 (2021).

[31] El-Kaderi, H. M. *et al.* Designed synthesis of 3d covalent organic frameworks. *Science* **316**, 268–272 (2007).

[32] Dong, Y.-B., Guan, Q. & Zhou, L.-L. Metalated covalent organic frameworks: from synthetic strategies to diverse applications. *Chemical Society Reviews* **51**, 6307 (2022).

[33] Erba, A. *et al.* CRYSTAL23: A program for computational solid state physics and chemistry. *Journal of Chemical Theory and Computation* **19**, 6891–6932 (2023).

[34] Dovesi, R. *et al.* *CRYSTAL23 User's Manual*. University of Torino, Torino (2023).

[35] Zhao, Y. & Truhlar, D. G. The m06 suite of density functionals for main group thermochemistry, thermochemical kinetics, noncovalent interactions, excited states, and transition elements: two new functionals and systematic testing of four m06-class functionals and 12 other functionals. *Theoretical Chemistry Accounts* **120**, 215–241 (2008).

[36] Vilela Oliveira, D., Laun, J., Peintinger, M. F. & Bredow, T. BSSE-correction scheme for consistent gaussian basis sets of double- and triple-zeta valence with polarization quality for solid-state calculations. *Journal of Computational Chemistry* **40**, 2364–2376 (2019).

[37] Laun, J. & Bredow, T. BSSE-corrected consistent gaussian basis sets of triple-zeta valence with polarization quality of the fifth period for solid-state calculations. *Journal of Computational Chemistry* **43**, 839–846 (2022).

[38] Mardirossian, N. & Head-Gordon, M. Thirty years of density functional theory in computational chemistry: an overview and extensive assessment of 200 density functionals. *Molecular Physics* **115**, 2315–2372 (2017).

[39] Heyd, J., Scuseria, G. E. & Ernzerhof, M. Hybrid functionals based on a screened coulomb potential. *The Journal of Chemical Physics* **118**, 8207–8215 (2003).

[40] Krukau, A. V., Vydrov, O. A., Izmaylov, A. F. & Scuseria, G. E. Influence of the exchange screening parameter on the performance of screened hybrid functionals. *The Journal of Chemical Physics* **125**, 224106 (2006).

[41] Grimme, S., Antony, J., Ehrlich, S. & Krieg, H. A consistent and accurate ab initio parametrization of density functional dispersion correction (dft-d) for the 94 elements h-pu. *The Journal of Chemical Physics* **132**, 154104 (2010).

[42] Borlido, P. *et al.* Exchange-correlation functionals for band gaps of solids: benchmark, reparametrization and machine learning. *npj Computational Materials* **6**, 1–17 (2020).

[43] Gale, J. D. & Rohl, A. L. The general utility lattice program (GULP). *Molecular Simulation* **29**, 291–341 (2003).

[44] BIOVIA, Dassault Systèmes. *Materials Studio 2022* (San Diego: Dassault Systèmes, 2022).

[45] Winn, J. S. The fugacity of a van der Waals gas. *Journal of Chemical Education* **65**, 772 (1988).

[46] Hinuma, Y., Pizzi, G., Kumagai, Y., Oba, F. & Tanaka, I. Band structure diagram paths based on crystallography. *Computational Material Science* **128**, 140–184 (2017).

[47] U.S. Geological Survey. Mineral commodity summaries 2025. Tech. Rep., U.S. Geological Survey (2025).

[48] Linstrom, P. J. & Mallard, W. G. The NIST chemistry WebBook: A chemical data resource on the internet. *Journal of Chemical & Engineering Data* **46**, 1059–1063 (2001).

Supplementary Information (SI)

Ferrocene-functionalized covalent organic frameworks exceeding the ultimate hydrogen storage targets: a first-principles multiscale computational study

Marcus Djokic^a and Jose L. Mendoza-Cortes^{a,b,*}

^a Department of Chemical Engineering and Materials Science, Michigan State University, East Lansing, MI 48824, USA

^b Department of Physics and Astronomy, Michigan State University, East Lansing, MI 48824, USA

* E-mail: jmendoza@msu.edu

CONTENTS

I. Introduction	1
A. Covalent organic frameworks for hydrogen storage	1
B. Metallocene chemistry and hydrogen binding	1
C. Transition metals in COFs: cost considerations	2
D. Design of MSUCOF-4-FeCp	2
II. Computational methods	4
A. Quantum mechanical calculations	4
1. Fragment calculations for force field development	4
2. Periodic framework calculations	4
B. Force field development and validation	4
C. Grand Canonical Monte Carlo simulations	5
D. Equation of state	5
III. Results and discussion	5
A. Structural properties and design validation	5
B. Electronic structure calculations	5
C. Hydrogen storage performance	6
D. Binding energy analysis and mechanisms	8
E. Practical considerations	11
Conclusions	11
Supplementary Information	11
Acknowledgements	11
Author contributions	11
Competing interests	12
Data availability	12
References	12

S1. Surface Area and Pore Volume	S16
S2. Force Field Fitting	S17
S3. Isotherm Plots	S18
S4. Hydrogen Density In MSUCOFs	S19
S5. Energy Distribution Peak Deconvolution	S21
S6. Optimized Geometries	S22
A. IRCOF-102	S22
B. MSUCOF-4	S23
C. MSUCOF-4-FeCp	S24

S1. SURFACE AREA AND PORE VOLUME

Surface areas and pore volumes were calculated using the Atom Volumes & Surfaces tool in Materials Studio.[44] The van der Waals (VdW) surface is constructed by rolling a spherical probe across the framework atoms, where the probe radius is defined by the adsorbate of interest. For hydrogen storage applications, a probe radius of 1.445 Å was used, corresponding to half the kinetic diameter of H₂ (2.89 Å). The resulting VdW surface (Fig. S1) delineates the accessible pore volume and the surface area available for hydrogen adsorption. This approach provides a consistent basis for comparing geometric properties across the IRCOF-102, MSUCOF-4, and MSUCOF-4-FeCp frameworks.

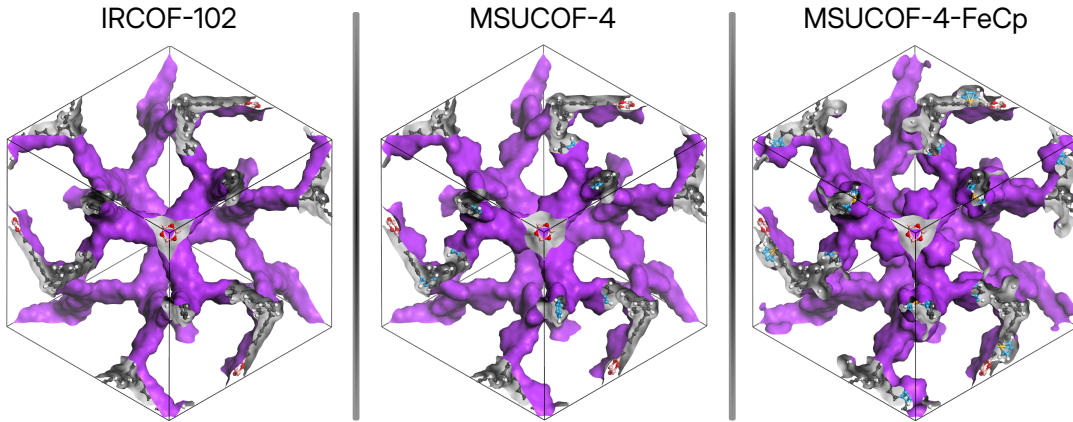


FIG. S1. Van der Waal surface (in purple) projected onto IRCOF-102, MSUCOF-4, and MSUCOF-4-FeCp. This surface is used for pore volume and surface area calculations.

S2. FORCE FIELD FITTING

Ferrocene adopts two limiting conformations: eclipsed and staggered, with the latter slightly favored in isolation. However, within the MSUCOF-4-FeCp framework, the spatial constraints imposed by the neighboring struts stabilize the eclipsed conformation. Therefore, both conformers were included in the force field training set to ensure transferability.

The initial H_2 binding configurations were identified using the Adsorption Locator tool in Materials Studio [44] which uses Monte Carlo sampling to locate energetically favorable adsorption sites. A random selection of these configurations was extracted, spanning various H_2 distances and orientations relative to the ferrocene center, for quantum mechanical refinement (Fig. S2).

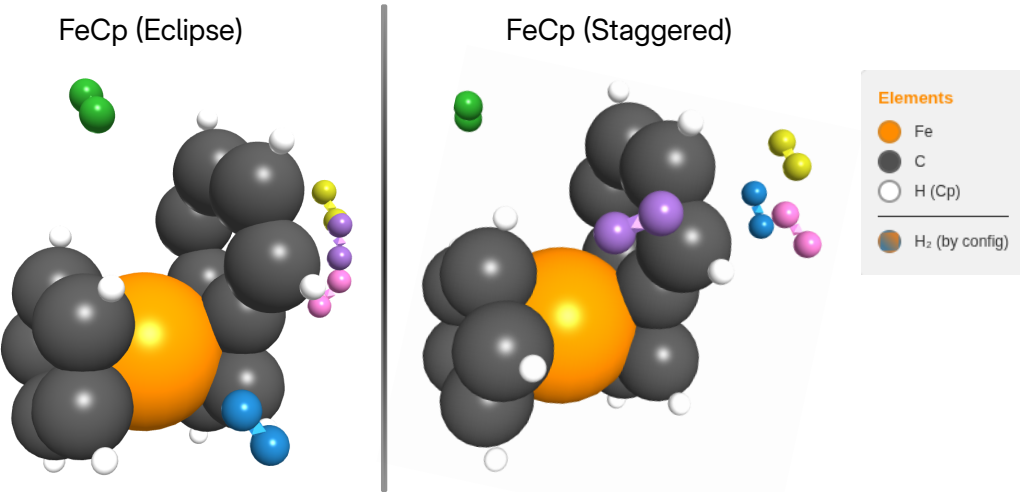


FIG. S2. We show example configurations that were used in the training of the QM-based force field fitting. Only the top 5 configuration are shown for display purposes. Note the hydrogen molecules are colored based on the configuration displayed.

Fragment calculations were performed following the methodology described in Section 2.1.1 of the main text. Vibrational frequency analysis confirmed the absence of imaginary frequencies and provided thermodynamic corrections, including zero-point energy (ZPE) and vibrational enthalpy (ΔH_{vib}^o). Binding enthalpies were calculated as follows:

$$\Delta H_{bind}^o = \Delta H_{Linker+\text{H}_2}^o - \Delta H_{Linker}^o - \Delta H_{\text{H}_2}^o \quad (\text{S12})$$

where ΔH^o represents the sum of the electronic energy, ZPE, and the correction of the vibrational enthalpy. The resulting QM binding energies were used to parameterize the Morse potentials using least-squares fitting in GULP, [43] achieving mean absolute errors below 0.5 kJ mol^{-1} (Fig. 3).

S3. ISOTHERM PLOTS

For completeness, we present the excess uptake isotherms (Fig. S3) to complement the total and net uptake data in the main text. The distinction between these metrics deserves clarification.

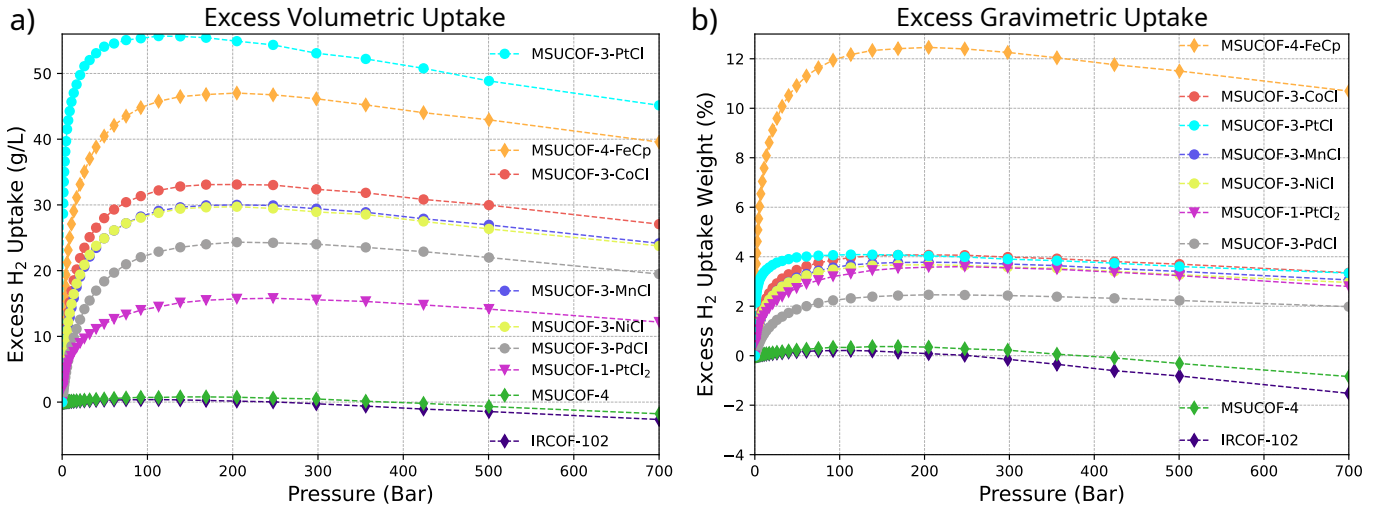


FIG. S3. Comparison of excess (a) volumetric and (b) gravimetric uptake at 298 K for the MSUCOF-4 family against top-performing MSUCOF variants. Excess uptake subtracts the bulk H₂ density corresponding to the pore volume, whereas net uptake (main text) applies a stricter correction using the full unit cell volume.

Net uptake subtracts the amount of H₂ that would occupy the entire volume of the unit cell if no framework was present (i.e., bulk gas under equivalent conditions). This metric directly quantifies the storage advantage of incorporating a porous material versus an empty tank of identical dimensions, making it the most rigorous computational benchmark. By contrast, excess uptake subtracts only the bulk H₂ that would occupy the accessible pore volume, excluding the volume displaced by the framework atoms.

From an experimental standpoint, excess uptake more closely reflects what is measured in typical adsorption experiments, as isolating the contribution of the full unit cell volume is not straightforward. However, computationally derived excess uptake is sensitive to how the pore volume is defined; specifically the choice of probe radius and van der Waals surface construction. Net uptake avoids this ambiguity by using the crystallographically defined unit cell volume. Hydrogen density values at each pressure and temperature were obtained from the NIST Chemistry WebBook.[48]

S4. HYDROGEN DENSITY IN MSUCOFS

Hydrogen density fields provide spatial insight into adsorption behavior that complements the isotherm data. These fields (Fig. S4) were generated using the Sorption module in Materials Studio,[44] where the local H₂ density at each point in the grid is calculated by averaging the count of sorbates over the associated volume element during the GCMC sampling.

At low pressure (1 bar), minimal H₂ loading is observed in all three frameworks. IRCOF-102 and MSUCOF-4 show negligible density throughout the pores, while MSUCOF-4-FeCp already exhibits a low but discernible density (blue regions, $< 5 \times 10^{-2}$ molecules Å⁻³) localized near the ferrocene centers and tritopic binding regions. This early-stage preferential adsorption reflects the enhanced binding affinity of the Fe sites.

At an intermediate pressure (10 bar), the contrast becomes pronounced. The pristine IRCOF-102 and MSUCOF-4 frameworks show only modest increases in H₂ density, with adsorption still diffuse throughout the pore volume. In contrast, MSUCOF-4-FeCp displays significant saturation of the ferrocene coordination sites, evidenced by elevated densities (green-red regions, $> 5 \times 10^{-2}$ molecules Å⁻³) concentrated around the FeCp moieties, while the remainder of the pores transition to a uniformly low density (blue). This spatial heterogeneity confirms that the ferrocene sites serve as primary adsorption centers.

At 30 bar, the pristine IRCOF-102 and MSUCOF-4 begin to show appreciable loading, with density accumulating near the framework surfaces and tritopic regions. However, MSUCOF-4-FeCp exhibits substantially higher saturation throughout, with the ferrocene sites approaching capacity. Relative hydrogen densities follow a clear hierarchy: MSUCOF-4-FeCp \gg MSUCOF-4 > IRCOF-102, consistent with isotherm data and confirming that ferrocene functionalization dramatically improves H₂ uptake at moderate pressures.

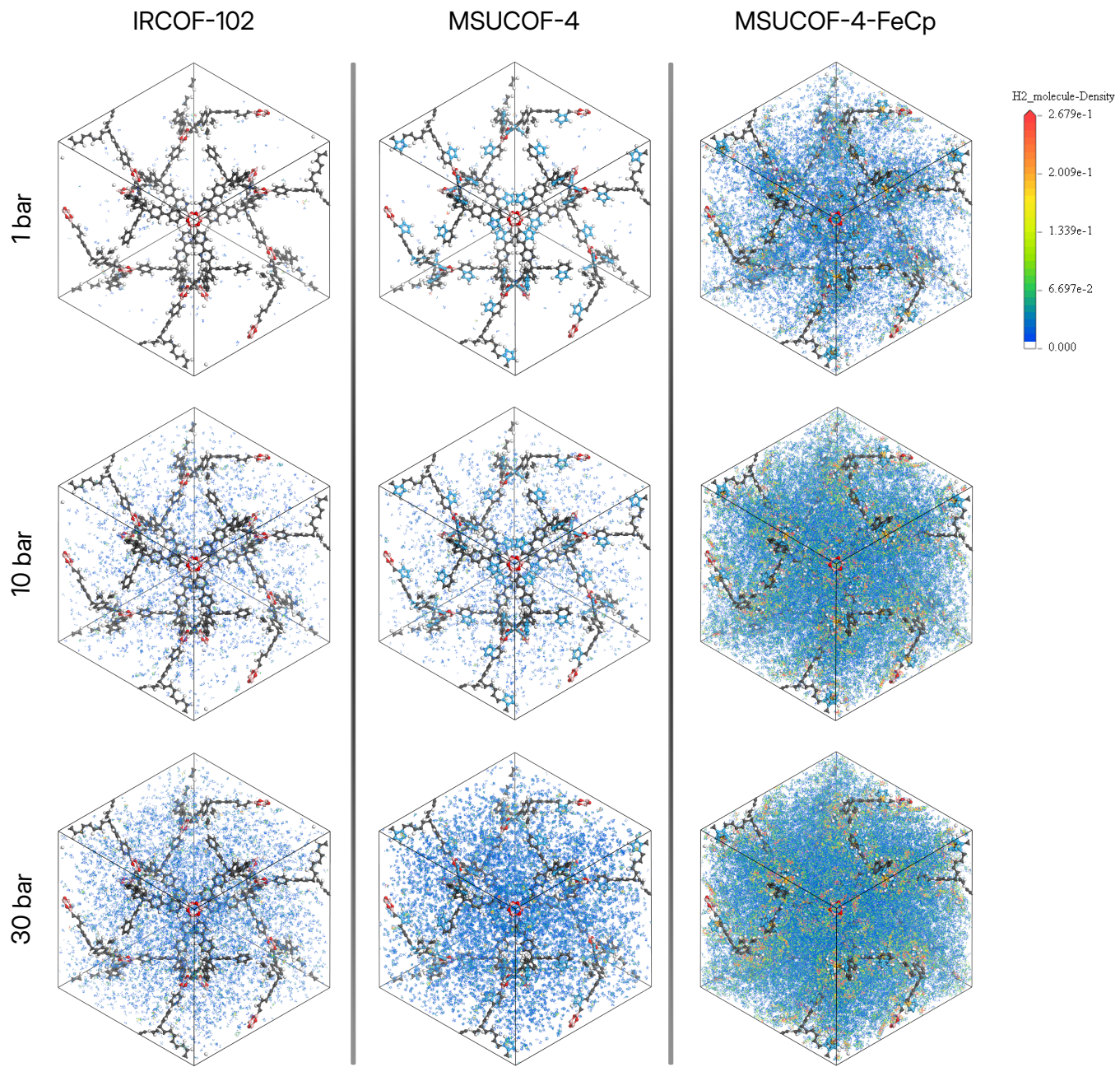


FIG. S4. Hydrogen density field displayed in IRCOF-102, MSUCOF-4, and MSUCOF-4-FeCp. The hydrogen density field is colored according to the rainbow legend. The fields are shown at various pressures (1, 10, and 30 bar) to demonstrate how the fields change upon further loading.

55. ENERGY DISTRIBUTION PEAK DECONVOLUTION

Table S1 provides an extended breakdown of the energy distribution analysis summarized in the main text (Table 2). Although the main manuscript reports ensemble-averaged quantities ($\langle E \rangle$, Q_{st} , σ) and the total number of resolved peaks, this table details the individual parameters for each deconvoluted peak obtained by fitting asymmetric Gaussian functions to the interaction energy distributions.

For each peak i , we report the center energy (μ_i), the fraction of adsorbed H₂ molecules associated with that binding mode (f_i), the site-specific isosteric heat ($Q_{st,i} = -\mu_i$), the full width at half maximum (FWHM) characterizing the breadth of the binding environment, and the energy boundaries used for integration. Peaks are classified as “Main” when they correspond to primary binding sites (e.g., metal centers, tritopic regions) or “Secondary” when they reflect weaker interactions such as shielded configurations, H₂–H₂ interactions or bulk-like pore filling.

The emergence of multiple peaks at elevated pressures reflects the sequential saturation of binding sites, with primary sites filling first followed by progressively weaker secondary sites. This detailed breakdown enables quantitative assessment of how each binding mode contributes to the overall adsorption behavior.

TABLE S1. Detailed peak deconvolution parameters from energy distribution analysis of GCMC simulations at 298 K. μ_i : peak center energy; f_i : fraction of H₂ molecules in peak i ; $Q_{st,i}$: site-specific isosteric heat; FWHM: full width at half maximum; Boundary: integration limits for each peak.

Material	P (bar)	Peak	Type	μ_i (kJ mol ⁻¹)	f_i	$Q_{st,i}$ (kJ mol ⁻¹)	FWHM (kJ mol ⁻¹)	Boundary (kJ mol ⁻¹)
<i>Low pressure (1 bar)</i>								
MSUCOF-1-PtCl ₂	1	1	Main	-21.13	0.86	22.15	7.09	[-25.3, 4.8]
MSUCOF-1-PtCl ₂	1	2	Secondary	-0.63	0.14	0.21	12.61	[-2.7, 4.8]
MSUCOF-3-CoCl	1	1	Main	-15.69	0.97	16.29	5.76	[-19.9, 4.0]
MSUCOF-3-MnCl	1	1	Main	-15.27	0.97	16.03	5.93	[-19.5, 3.6]
MSUCOF-3-NiCl	1	1	Main	-16.95	0.97	17.22	6.52	[-22.4, 6.5]
MSUCOF-3-PdCl	1	1	Main	-12.76	0.99	12.81	6.03	[-16.9, 4.8]
MSUCOF-3-PtCl	1	1	Main	-27.82	1.01	27.64	11.22	[-37.0, 0.2]
MSUCOF-4-FeCp	1	1	Main	-19.46	1.00	18.10	11.45	[-29.5, 1.0]
<i>Intermediate pressure (17.1 bar)</i>								
MSUCOF-1-PtCl ₂	17.1	1	Main	-16.95	0.82	20.06	12.00	[-25.7, 8.6]
MSUCOF-1-PtCl ₂	17.1	2	Secondary	-4.39	0.13	3.14	4.79	[-7.3, -3.1]
MSUCOF-1-PtCl ₂	17.1	3	Secondary	-0.63	0.06	0.30	1.32	[-7.3, 8.6]
MSUCOF-3-CoCl	17.1	1	Main	-15.69	0.76	15.73	5.21	[-20.3, 7.3]
MSUCOF-3-CoCl	17.1	2	Main	-9.83	0.24	8.66	5.22	[-10.3, 7.3]
MSUCOF-3-MnCl	17.1	1	Main	-15.27	0.99	15.70	7.28	[-19.9, 6.5]
MSUCOF-3-NiCl	17.1	1	Main	-16.11	0.98	16.55	8.00	[-23.2, 6.9]
MSUCOF-3-PdCl	17.1	1	Main	-12.34	1.00	12.78	6.66	[-17.4, 8.6]
MSUCOF-3-PtCl	17.1	1	Main	-23.64	1.01	24.86	13.54	[-37.4, 2.3]
MSUCOF-4-FeCp	17.1	1	Main	-15.69	1.02	15.16	13.23	[-30.3, 6.9]
<i>High pressure (700 bar)</i>								
MSUCOF-1-PtCl ₂	700	1	Main	-1.46	0.78	1.14	6.68	[-25.7, 15.7]
MSUCOF-3-CoCl	700	1	Main	-14.85	0.91	14.90	8.97	[-21.1, 10.3]
MSUCOF-3-CoCl	700	2	Secondary	-8.16	0.10	8.06	3.05	[-9.4, 10.3]
MSUCOF-3-MnCl	700	1	Main	-14.02	0.93	14.35	9.17	[-20.7, 11.5]
MSUCOF-3-MnCl	700	2	Secondary	-6.49	0.08	6.51	2.73	[-7.7, 11.5]
MSUCOF-3-NiCl	700	1	Main	-14.02	0.58	14.54	6.69	[-23.6, 11.9]
MSUCOF-3-NiCl	700	2	Main	-5.65	0.42	5.89	8.64	[-6.9, 11.9]
MSUCOF-3-PdCl	700	1	Main	-11.92	0.93	12.09	8.17	[-18.2, 11.5]
MSUCOF-3-PdCl	700	2	Secondary	-6.07	0.08	5.79	2.69	[-6.9, 11.5]
MSUCOF-3-PtCl	700	1	Main	-21.97	0.87	22.74	13.15	[-37.9, 7.7]
MSUCOF-3-PtCl	700	2	Secondary	-12.76	0.13	12.50	5.38	[-15.3, 7.7]
MSUCOF-4-FeCp	700	1	Main	-13.18	0.83	13.08	13.19	[-30.8, -11.5]
MSUCOF-4-FeCp	700	2	Main	-7.74	0.17	7.80	3.34	[-30.8, 10.7]

S6. OPTIMIZED GEOMETRIES

Here we report the optimized structures obtained at the hybrid-DFT level of theory (HSE06-D3).

A. IRCOF-102

```

data_IRCOF102
_cell_length_a    42.955631
_cell_length_b    42.955631
_cell_length_c    42.955631
_cell_angle_alpha 90.000000
_cell_angle_beta  90.000000
_cell_angle_gamma 90.000000
_space_group_name_H-M_alt      'I -4 3 d'
_space_group_IT_number        220
loop_
_atom_site_label
_atom_site_type_symbol
_atom_site_fract_x
_atom_site_fract_y
_atom_site_fract_z
O1      O    0.210053  -0.195275  0.260431
H1      H    0.049110  -0.208302  0.118102
H2      H    0.109203  -0.280245  0.222018
H3      H    0.095876  -0.203198  0.150390
H4      H    0.014119  -0.278596  0.179640
H5      H    0.153924  -0.272298  0.257309
H6      H    0.060078  -0.272257  0.213170
C1      C    0.028534  -0.244580  0.145792
C2      C    0.032412  -0.262350  0.172908
C3      C    0.058413  -0.258813  0.191739
C4      C    0.077914  -0.219722  0.157247
C5      C    0.081877  -0.237391  0.184295
C6      C    0.150987  -0.200698  0.224463
C7      C    0.051708  -0.223026  0.138554
H7      H    0.163010  -0.178361  0.224930
C8      C    0.120450  -0.257547  0.223164
C9      C    0.161779  -0.224795  0.243581
H8      H    0.116331  -0.185073  0.192053
C10     C    0.125032  -0.204616  0.205657
C11     C    0.109341  -0.233211  0.204465
C12     C    0.145846  -0.253224  0.242656
B1      B    0.189921  -0.219831  0.265204
C13     C    0.250000  0.375000  -0.000000

```

B. MSUCOF-4

```

data_MSUCOF-4
_cell_length_a      42.974269
_cell_length_b      42.974269
_cell_length_c      42.974269
_cell_angle_alpha   90.000000
_cell_angle_beta    90.000000
_cell_angle_gamma   90.000000
_space_group_name_H-M_alt      'I -4 3 d'
_space_group_IT_number        220
loop_
_atom_site_label
_atom_site_type_symbol
_atom_site_fract_x
_atom_site_fract_y
_atom_site_fract_z
H1      H      -0.158135  0.237213  0.179336
H2      H      -0.126859  0.206083  0.135292
C1      C      -0.173131  0.198626  0.113882
C2      C      -0.168023  0.225856  0.159030
C3      C      -0.151879  0.209499  0.136080
H3      H      -0.167510  0.186439  0.092456
O1      O      -0.199299  0.256263  0.215188
H4      H      -0.209918  0.116670  0.050006
H5      H      -0.282069  0.214545  0.114075
H6      H      -0.277727  0.180318  0.013834
H7      H      -0.271326  0.213562  0.060219
H8      H      -0.275895  0.247437  0.160607
H9      H      -0.205337  0.148686  0.097424
C4      C      -0.261937  0.173155  0.032343
C5      C      -0.237545  0.183681  0.082152
C6      C      -0.244714  0.145663  0.028660
C7      C      -0.223996  0.137589  0.052318
C8      C      -0.226409  0.240157  0.165058
C9      C      -0.204132  0.207996  0.123301
C10     C      -0.258430  0.191802  0.058482
C11     C      -0.233334  0.203390  0.109804
C12     C      -0.220766  0.156008  0.078699
C13     C      -0.255529  0.236332  0.150353
C14     C      -0.200907  0.225605  0.151186
B1      B      -0.223173  0.260696  0.194234
C15     C      -0.258998  0.218213  0.123924
C16     C      0.375000  -0.000000  0.250000

```

C. MSUCOF-4-FeCp

```

data_MSUCOF-4-FeCp
_cell_length_a    43.072089
_cell_length_b    43.072089
_cell_length_c    43.072089
_cell_angle_alpha 90.000000
_cell_angle_beta  90.000000
_cell_angle_gamma 90.000000
_space_group_name_H-M_alt      'I -4 3 d'
_space_group_IT_number        220
loop_
_atom_site_label
_atom_site_type_symbol
_atom_site_fract_x
_atom_site_fract_y
_atom_site_fract_z
H1      H    -0.134982  0.149227  0.179180
H2      H    -0.231777  0.146943  0.148759
H3      H    -0.227735  0.185645  0.197590
H4      H    -0.174239  0.123904  0.137467
C1      C    -0.159911  0.152672  0.178400
C2      C    -0.177526  0.172131  0.198639
C3      C    -0.180697  0.139432  0.156223
Fe1     Fe   -0.181730  0.186482  0.154303
H5      H    -0.155773  0.241797  0.175299
C4      C    -0.211072  0.150953  0.162574
H6      H    -0.124740  0.208608  0.132020
C5      C    -0.171328  0.200853  0.110626
C6      C    -0.165725  0.230594  0.155072
C7      C    -0.149520  0.213107  0.132201
H7      H    -0.165942  0.186504  0.090680
H8      H    -0.168335  0.186405  0.217235
O1      O    -0.197264  0.258616  0.211833
H9      H    -0.208529  0.118346  0.049133
H10     H    -0.280252  0.215410  0.113213
C8      C    -0.209070  0.171176  0.188773
H11     H    -0.278985  0.179179  0.013835
H12     H    -0.271923  0.213677  0.059128
H13     H    -0.273482  0.249930  0.158721
H14     H    -0.202769  0.152028  0.095268
C9      C    -0.262580  0.172844  0.032031
C10     C    -0.236742  0.185275  0.080468
C11     C    -0.244752  0.145810  0.028432
C12     C    -0.223084  0.138868  0.051471
C13     C    -0.224519  0.244384  0.161746
C14     C    -0.201644  0.211641  0.119487
C15     C    -0.258673  0.192194  0.057473
C16     C    -0.232184  0.205807  0.107339
C17     C    -0.219291  0.158094  0.077119
C18     C    -0.253026  0.239326  0.148211
C19     C    -0.198044  0.230386  0.147118
B1      B    -0.221218  0.264045  0.191289
C20     C    -0.256908  0.220033  0.121792
C21     C    0.375000  0.000000  0.250000

```